

# Nanoscale analysis of surface oxides on ZnMgAl hot-dip-coated steel sheets

M. Arndt · J. Duchoslav · H. Itani · G. Hesser ·  
C. K. Riener · G. Angeli · K. Preis · D. Stifter ·  
K. Hingerl

Received: 11 August 2011 / Revised: 13 September 2011 / Accepted: 16 October 2011 / Published online: 17 November 2011  
© Springer-Verlag 2011

**Abstract** In this work, the first few nanometres of the surface of ZnMgAl hot-dip-galvanized steel sheets were analysed by scanning Auger electron spectroscopy, angle-resolved X-ray photoelectron spectroscopy and atomic force microscopy. Although the ZnMgAl coating itself is exhibiting a complex micro-structure composed of several different phases, it is shown that the topmost surface is covered by a smooth, homogeneous oxide layer consisting of a mixture of magnesium oxide and aluminium oxide, exhibiting a higher amount of magnesium than aluminium and a total film thickness of 4.5 to 5 nm. Especially by the combined analytical approach of surface-sensitive methods, it is directly demonstrated for the first time that within surface imprints—created by industrial skin rolling of the steel sheet which ensures a smooth surface appearance as well as reduced yield-point phenomenon—the original, smooth oxide layer is partly removed and that a layer of native oxides, exactly corresponding to the chemical structure of the underlying metal phases, is formed.

**Keywords** Hot-dip galvanizing · ZnMgAl-coating · Surface characterisation · Auger electron spectroscopy · X-ray photoelectron spectroscopy · Atomic force microscopy

## Introduction

Hot-dip galvanizing is an effective method for the corrosion protection of steel surfaces and makes steel applicable as the most important raw material for the automotive, building and household appliance industry. In the last 35 years, considerable research efforts were undertaken to improve the corrosion resistance of the zinc-based coatings by adding, e.g. magnesium and aluminium to form Zn–Mg–Al alloys, with typical values of the magnesium and aluminium concentrations in the zinc bath ranging from 0.1 up to 11.0 wt.% [1–8]. Within a variety of recent studies, it was shown that the corrosion protection of these ZnMgAl layers is significantly enhanced compared with standard hot dip galvanized Zn coatings [2, 3, 9–13].

Since corrosion attack mostly starts at the surface of the coating and not from the bulk, the exact knowledge of the initially formed surface with respect to the surface structure, surface morphology and chemical composition is crucial. However, in most of the to-date published papers only the corrosion behaviour was discussed on the basis of analysis of corrosion products formed on the surface and in the bulk of the coatings after salt spray tests. Moreover, there are only a few other scientific contributions within the literature that give a better understanding of the structure, the corrosion mechanisms and behaviour of Zn–Mg-coated steel originating, e.g. from electrodeposited Zn and consecutively physical-vapour-deposited Mg (PVD) [14–16], a system which might exhibit similarities to hot-dip-galvanized Zn–Mg–Al-coated steel sheets. In this context,

Published in the special paper collection on *Solid State Analysis (FKA 16)* with guest editor G. Friedbacher.

M. Arndt (✉) · J. Duchoslav · H. Itani · G. Hesser · D. Stifter ·  
K. Hingerl

Zentrum für Oberflächen- und Nanoanalytik (ZONA) und  
Christian Doppler Labor für mikroskopische und  
spektroskopische Materialcharakterisierung (CDL-MS-MACH),  
Johannes Kepler Universität Linz,  
Altenbergerstraße 69,  
4040 Linz, Austria  
e-mail: martin.arndt@jku.at

C. K. Riener · G. Angeli · K. Preis  
voestalpine Stahl GmbH,  
voestalpine-Straße 3,  
4031 Linz, Austria

Chen et al. [16] used this Zn–Mg PVD-coated steel system in an X-ray photoelectron spectroscopy (XPS) analysis and found a 5-nm thick layer of mostly MgO and its corrosion products on the surface. From other references [17–19], it is known that MgO is highly reactive with water and does not possess appropriate corrosion protection, whereas its mixtures with Al<sub>2</sub>O<sub>3</sub> forming, e.g. MgAl<sub>2</sub>O<sub>4</sub> are significantly more resistant.

Consequently, for a deeper understanding, we focus in this work for the first time on a full characterisation of the surface and subsurface layer of hot-dip-galvanized ZnMgAl coatings on steel sheets, which can only be obtained by a combined analytical approach using surface-sensitive methods. Moreover, the information about the formed surface structure will also play a key role for further understanding of differences in other important properties of such coatings—besides the reported excellent corrosion protection—from the viewpoint of the processability and applicability of the final product [20–22]. It shall be especially clarified in this work if the surface of the studied ZnMgAl coating system shows any analogy to the surface of standard hot-dip-galvanized steel with a homogeneous 5-nm-thick Al<sub>2</sub>O<sub>3</sub> layer on top [23, 24] or if the surface structure is similar to the PVD coated system analysed by Chen et al. [16], namely covered by a 5-nm thick Mg oxide layer. As a third possibility, the surface structure could also directly be related to the inner structure of the ZnMgAl material itself; from other works, it is well known that ZnMgAl-coating is not uniform but exhibits different phases [25–27], and therefore, the question arises if the surface oxides correspond to the underlying pattern of the ZnMgAl structure below the surface. Finally, a crucial aspect of this paper is dedicated to occurring modifications in the surface oxide structure on industrial samples resulting from the subsequent skin-rolling process performed on the final steel sheets.

## Experimental

### Sample material

All samples for this study were prepared at the production line of voestalpine Stahl GmbH by hot-dip galvanizing of cold-rolled steel sheets. The coating layers exhibit a thickness of about 8 μm, adjusted by air knives immediately after the dipping bath with a concentration of 96 wt.% Zn, 2 wt.% Mg and 2 wt.% Al. Furthermore, a part of the samples was subsequently subjected to a skin-passing procedure, a common process in the surface texturing of industrially produced steel sheets by imprinting a micron-scale topographic structure onto the coated steel surface.

Prior to the measurements, all samples were cut into pieces with dimension of 8×8 mm<sup>2</sup> and cleaned in an ultrasonic bath to remove adventitious surface contaminations (mostly carbon-based) originating from sample handling in the production line. Our experience has shown that only a rather complex cleaning procedure reliably removes these contaminations, which e.g. would render surface mapping by Auger electron spectroscopy (AES) impossible due to heavy carbon re-deposition on the surface in the area scanned by the electron beam. In detail, it has been tried to take Auger element mappings at first on ZnMgAl samples from the production line without any further treatment and second on samples after simple acetone and ethanol cleaning steps in an ultrasonic bath. For both cases, the carbon contamination on the scanned area was increasing with the number of subsequent scans. To prevent this type of contamination, the beaker used for cleaning in the ultrasonic bath is at first washed with a solution of 50% sulphuric acid and 50% hydrogen peroxide. For the following cleaning steps, the samples are consecutively placed for 15 min in organic solvents, namely tetrahydrofuran, isopropanol and ethanol, with each step carried out twice and by always using a fresh organic solvent.

### Analytical methods

The majority of the analytical work for this study was performed with a scanning AES Microscope JAMP 9500 F from JEOL, which is equipped with a Schottky field emitter and a hemispherical electron energy analyser to perform Auger measurements in the range from 0 to 2,500 eV with a spatial resolution down to 8 nm. As to the detector, the AES spectra are simultaneously recorded by seven channeltrons in parallel. Furthermore, an argon sputter gun with ion energies between 0.5 and 3 keV for sputter depth profiling is available. Alternatively, this gun can be used for charge neutralising by using ion energies between 10 and 50 eV.

As a second surface analytical method, a Thetaprobe system from Thermo Scientific was applied for performing angle-resolved (AR-)XPS measurements. The system is equipped with a monochromated AlK $\alpha$ -source with a beam focus adjustable between 30 and 400 μm and a dual flood gun (low-energy electrons and argon ions) for effective charge neutralisation. The angle-resolved data is simultaneously acquired in a range between 20° and 80° with respect to the sample surface normal by a 2D detector with 112 energy channels and 96 angle channels. AR-XPS data obtained in this way can subsequently be processed for the reconstruction of virtual, i.e. non-destructive, depth profiles of the topmost surface layers, being an option available in the Advantage software package provided by Thermo Scientific.

Further analytical and preparative tools used in this work comprise a 1540 XB focused ion beam (FIB) system from Zeiss for sample preparation and cutting, a 200 keV transmission electron microscope (TEM, JEOL-2011 system) as well as an atomic force microscope (AFM, Dimension 3100) from Veeco. The AFM was used in tapping mode, and the resulting scans were processed with gwyddion and ImageJ software.

For advanced analytical investigations and direct comparisons, Auger element mappings and AFM topography images of the same area could be achieved by first scanning an area with AFM and marking the region in the optical micrograph taken in the AFM. Afterwards, the sample was placed into the AES system in which secondary electron images were taken to identify the same area. After adjusting the sample rotation and magnification, complementary Auger element mappings were performed.

## Results

### General overview of coating structure

For initial characterization and obtaining general information on the fabricated ZnMgAl coatings, a cross-section of a typical layer was prepared by FIB-cutting of a 1- $\mu\text{m}$  thick lamella, which was mounted onto a copper grid and transferred for elemental mapping to the SAES system. As can be seen in Fig. 1 and as already previously reported [25–27], the coating exhibits a complex microstructure composed of several different phases, including a primary zinc phase (Zn-dendrites, also with embedded and very small Al precipitations), a binary eutectic consisting of zinc and the hard, intermetallic Laves phase  $\text{MgZn}_2$  [26], a ternary eutectic consisting of the former two phases including aluminium, which might also build up a dendrite structure on its own [27].

### AES sputter depth profiling

In order to clarify the nature of the topmost surface layer which is formed on the ZnMgAl coatings, sputter depth profiling by AES was performed. The depth profiles were made on different points on the cleaned surfaces, corresponding to regions with different phases of the sample. For these measurements, the primary electron beam parameters were set to 15 kV, 200 nA with a spot size of 1  $\mu\text{m}$ . In addition, the sample was tilted towards to the analyser so that the spectra can be regarded as more bulk-sensitive. The argon beam parameters for sputtering were set to 3 keV, corresponding to 25 nm etching per minute on  $\text{SiO}_2$ .

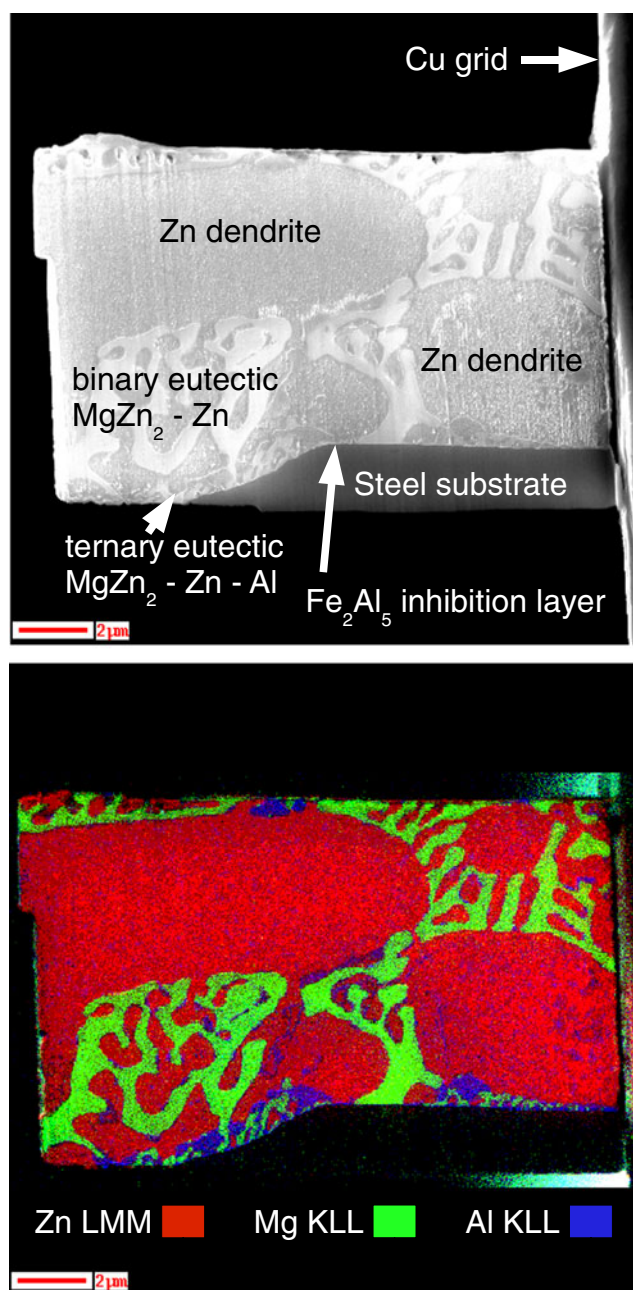


**Fig. 1** FIB lamella of a ZnMgAl coating on steel substrate. In the *upper* picture, a secondary electron image, and in the *lower* one, the corresponding Auger element mapping is shown

Each sputter cycle lasted for 5 s ( $\sim 2$  nm in  $\text{SiO}_2$ ) per cycle. After each sputter cycle, the spectra for all relevant elements were recorded with an energy resolution of the analyser set to  $\Delta E/E=0.1$  eV for obtaining high-resolution scans.

In Fig. 2, the first ten cycles of such a depth profile performed in a region with a ternary eutectic is shown. It is clearly seen that the oxygen peak is highest at the surface and then vanishing with increasing depth. This behaviour corresponds exactly to the evolution of the

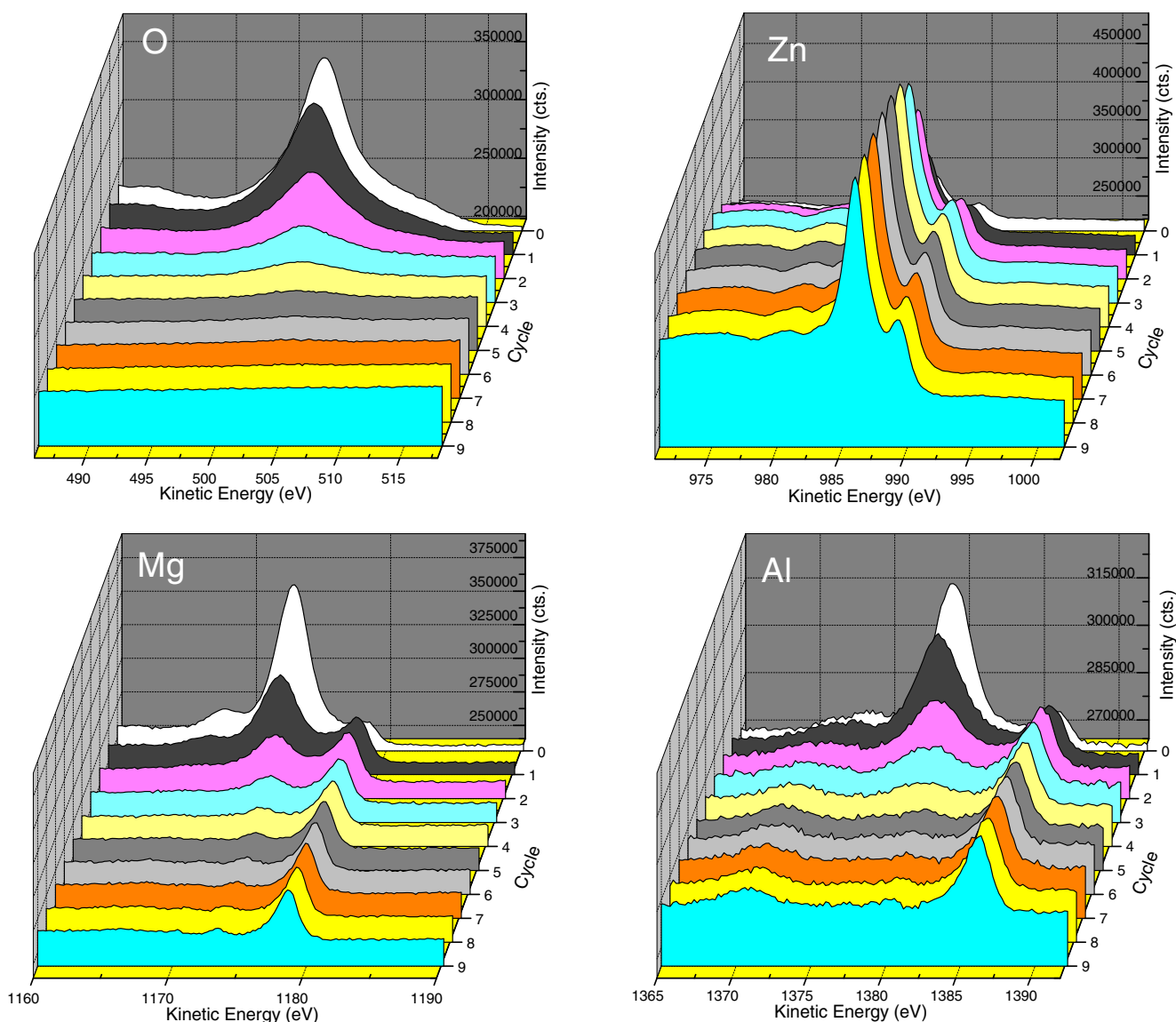


**Fig. 2** The first ten cycles of an AES sputter depth profile are given, with each sputter cycle being equivalent to an etching step of 2 nm in depth on  $\text{SiO}_2$ . The spectra in the background correspond to the surface and the ones in the front represent spectra when reaching into

the bulk. In the Mg and Al spectral range, oxide peaks located some electronvolts towards lower kinetic energies with respect to the metal peaks are disappearing with increasing depth. Zn could not be detected on the surface neither in elemental nor in oxidic form

oxide peaks of Mg and Al, which are shifted in the spectra by several electronvolts towards lower kinetic energies with respect to the metal peaks: The respective oxide peaks of Mg and Al disappear with increasing depth, whereas the metal peaks of Mg and Al emerge. In contrast, Zn does not exhibit an oxide peak, but a metallic peak emerges simultaneously with the disappearance of the oxides. Interestingly, depth profiles performed on the surface region of a Zn dendrite look identical within the first ten sputter cycles.

For a more detailed and quantitative analysis, the atomic concentration of the different elements—also divided into in their oxide and metal states—is plotted in Fig. 3 versus

the estimated sputter depth. In order to obtain the respective atomic concentrations, reference spectra for all species observed in the measured spectra were taken from the database supplied by JEOL, namely O from  $\text{MgO}$  and  $\text{Al}_2\text{O}_3$ , Zn metal, Mg from metallic Mg and  $\text{MgO}$  as well as Al from metallic Al and  $\text{Al}_2\text{O}_3$ . All spectra were then differentiated for background subtraction, and a linear least-square fitting routine for fitting the measured spectra with the reference data was carried out. The obtained concentrations were then summed up and normalised to yield 100% in total.

From the resulting diagram in Fig. 3, the presence of a mixed layer containing magnesium oxide and aluminium

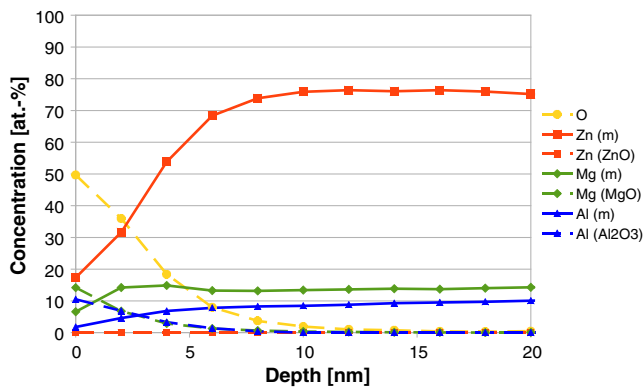


**Fig. 3** AES depth profile (with a sputter rate for SiO<sub>2</sub> since it is not practicable to define a sputter rate of a multi-component material) on a ZnMgAl surface splitted into different chemical states by fitting reference spectra by LLS

oxide is again confirmed, with a higher amount of Mg than Al (15% versus 10%). Below this oxide layer, Zn, Mg and Al are solely present in their metallic form.

### AES surface elemental mapping

In order to detect a potential influence of the underlying phases and intrinsic structures of the eutectics on the formed surface oxide layer, AES surface maps were performed. Already the AES depth profiles described above and carried out on different regions corresponding to the various phases observed in the ZnMgAl coatings hinted to a rather uniform distribution of Mg and Al in the topmost layer, as now exemplarily confirmed in the AES surface maps of Fig. 4, performed with a primary beam energy of 30 keV and an emission current of 10 nA.

The topmost left picture shows the secondary electron image of the analysed area. The observed area is not homogeneous but shows the typical structure of a ternary eutectic. Since the secondary electrons (SE) have a higher inelastic mean free path in matter due to their lower energy (<20 eV) when compared with

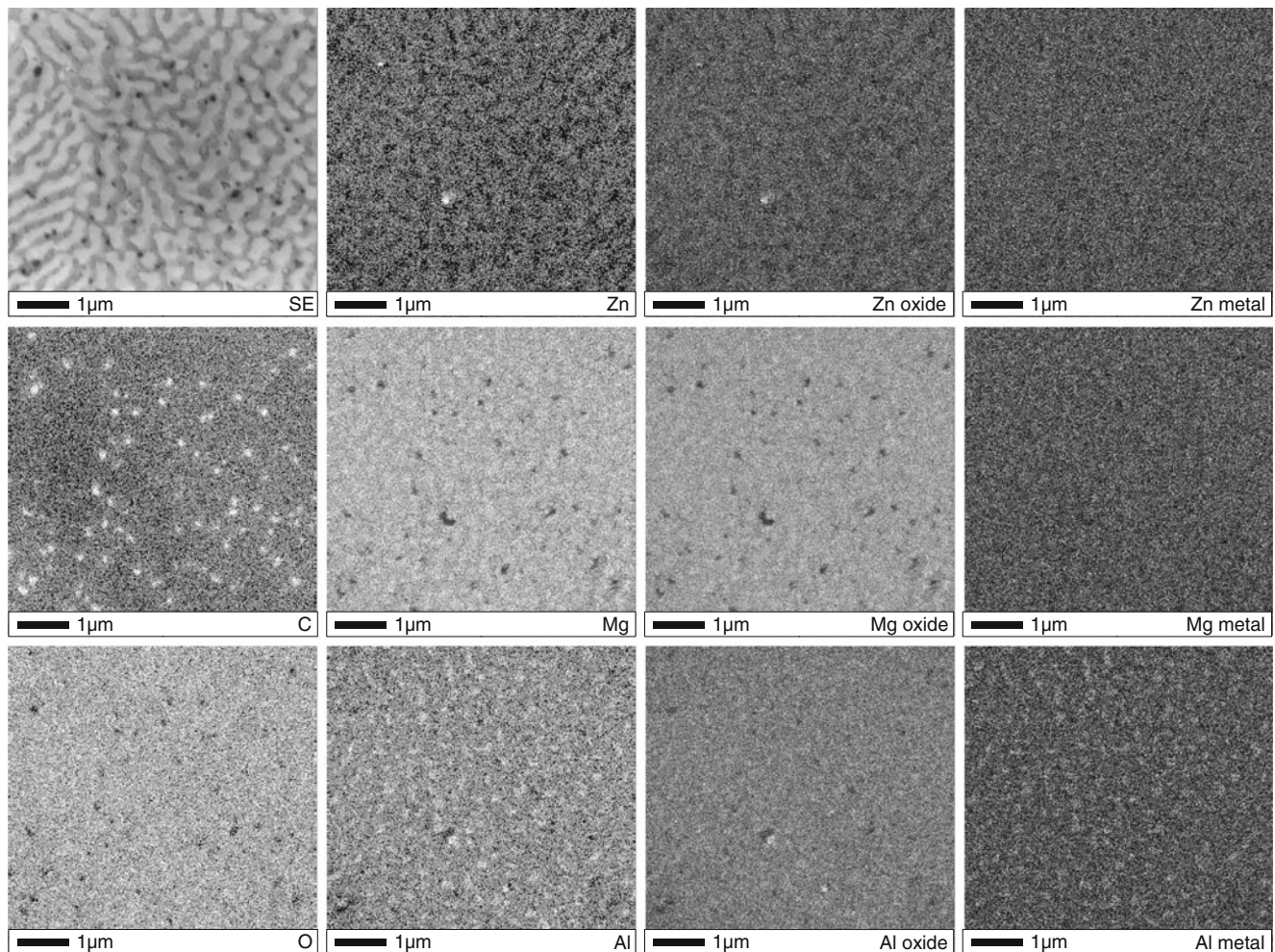


**Fig. 4** Elemental and chemical state AES mappings on a ternary eutectic. The Zn, Mg and Al mappings are split respectively into oxide and metal part. One can see that the Mg and the Al oxide are quite

uniformly spread over the area. The carbon particles stem from residual contaminations which could not be removed by the cleaning procedure

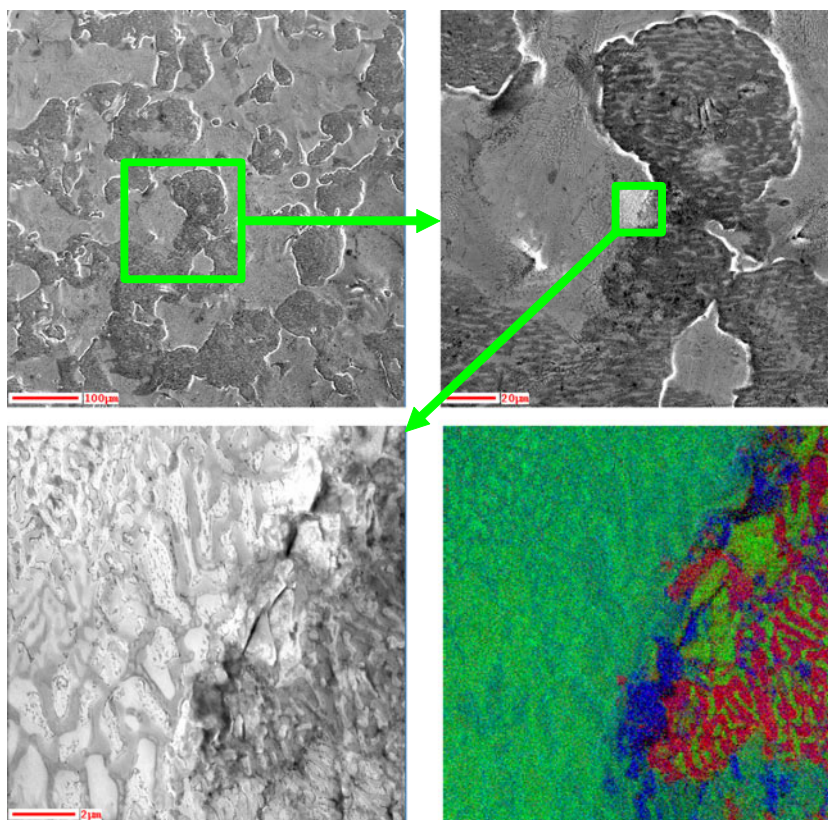
Auger electrons (for Zn, Mg and Al roughly 1, 1.2 and 1.4 keV), they are more bulk-sensitive than the Auger electrons. In contrast, since the sample surface was tilted for these measurements by  $60^\circ$  away from the detector, the information obtained from the Auger electrons is very surface-sensitive. In addition, the mapping was performed in constant analyser energy mode with the pass energy chosen in such a way that one channeltron of the detector recorded the signal of a metal peak whereas a second channeltron was covering the corresponding oxide peak for a subsequent discrimination of oxidised and metallic state. The remaining channeltrons covering higher energy ranges were used for recording the background. The intensity scale in the resulting images of Fig. 4 is therefore defined as  $I = (P - B) / (P + B)$ , with  $P$  defined as peak signal intensity and  $B$  being the intensity recorded on the background position.

In contrast to the SE image, the results of the AES maps of Fig. 4 show that the Mg and Al oxides are homogeneously distributed and do not follow the underlying eutectic structure of the bulk. Similar mappings were carried out also on other areas of the surface (not shown here) with the same result of confirming a uniformly distributed MgAl oxide layer.

#### AES element mappings on industrial sample surface

Skin-rolling is a standard processing step in the steel production industry. Consequently, analogous AES analytics was carried out for skin passed surfaces, as depicted in Fig. 5. The darker areas visible in the SE images correspond to imprints with a depth of about  $2 \mu\text{m}$  and with lateral extensions in the order of magnitude of  $100 \mu\text{m}$ . For a direct comparison of the different surface regions, AES mapping was performed close to an edge of an imprinted region. The results of the AES mappings are shown on the lower right picture of Fig. 5, where an overlay of the mappings of Zn (red), Mg (green) and Al (blue) is presented (mappings of C and O not shown). One can clearly see on the left side of the image that a homogeneous mixture of Al and Mg, as observed before on the non-skin passed surface, is present since, in this area, there is no structural correlation to the underlying metal structure, which is visible in the corresponding SE image on the corresponding lower left picture. In contrast, in the imprinted region a direct correspondence between the structure of the eutectic observed by SE and the detected elemental distribution, with Zn represented by the red colour, becomes visible. These results directly show that the skin passing process breaks up and partly

**Fig. 5** AES element mapping of a skin passed surface with overview SE images in the upper row. The lower right picture shows the overlay of the Zn, Mg and Al AES mapping (Zn: red, Mg: green, Al: blue), whereas the lower left one depicts the corresponding SE image of the same region



removes the primarily existent MgAl oxide layer in the imprints and that subsequently the native oxides of the different phases are formed on the surface.

### AFM investigations

For a more thorough investigation of the effect of skin passing on the surface structure, AFM scans were performed to compare the topography of the pristine MgAl oxide covered surface with the surface in the imprints.

In Fig. 6, the results of the performed AFM scans of different regions are shown. On positions 2 and 4 (Root mean square roughness values (rms) are 24.4 and 14.5 nm, respectively), located on the plateaus, the surface is evidently much smoother than in the valleys as measured on positions 1 and 3 (rms, 45.2 and 60.9 nm), where native oxides of Zn, Mg and Al formed due to the direct contact with air after skin passing. Interestingly, the measurement taken from position 1, although being located in an imprinted region, also exhibits in the middle of the scanned area a rather smooth feature. The same area, which was investigated by AFM was therefore analysed by AES (Fig. 7), showing that the original smooth and uniform MgAl oxide layer is broken up by the skin passing procedure and that small remaining flakes are pressed into the coating: The smooth area in the AFM scan matches exactly the cyan colour of the AES mapping which proves the existence of the MgAl oxide layer, also observable as brighter region in the SE image. In contrast, the rougher topography of the AFM images exactly corresponds to the region with surface imprints and in such areas only native oxide structures could be observed.

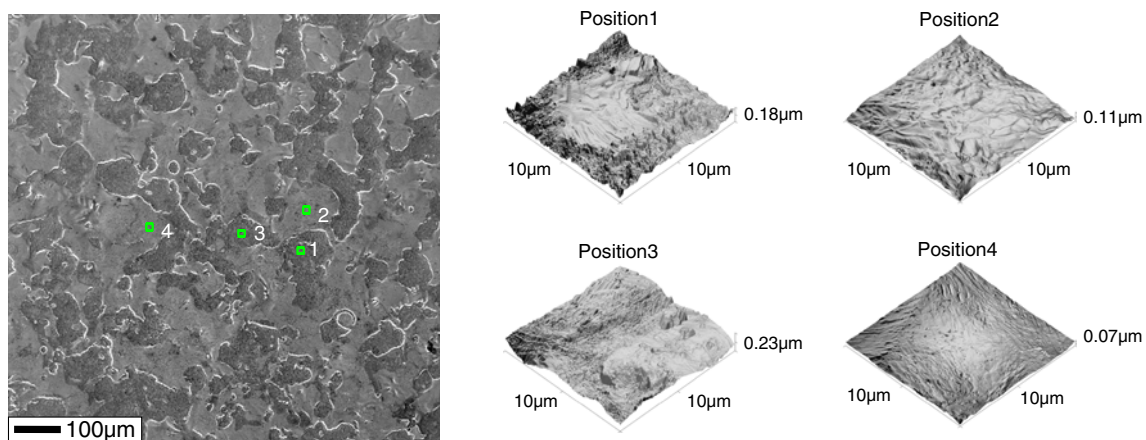


**Fig. 6** AFM topography scans in different regions on the surface of a skin passed ZnMgAl-coated steel sheet. The positions are shown in the SE image on the *left*. Positions 1 and 3 are located in the imprint

### ARXPS non-destructive depth profiles

In order to answer the question of the exact thickness of the observed pristine MgAl oxide layer, AR-XPS analysis was performed, since the above presented AES depth profiles gave only an approximate idea, due to the unknown sputter rate for the present material.

The XPS measurements were solely performed on non-skin passed samples, due to the rather extended spot of the used X-ray source.

In Fig. 8, a so-called relative depth plot of the surface elements that were found via XPS is depicted, giving an average depth position of each element relative to the others. The plot was calculated from the angle-resolved data of Fig. 9a, comprising six different angles, by taking the logarithm of the ratio between the bulk-sensitive angles and the surface-sensitive angles. As one can see, the surface is covered by a carbon contamination, whereas below a mixture of O, Mg and Al is found, with Zn being finally located in the bulk.

For further calculations, a simple three-layer model was defined, with Zn bulk material covered by a MgAl oxide layer and a carbon contamination film on top. Again, the AR data of Fig. 9a is taken, and a virtual depth profile is reconstructed in an iterative way according to the Lambert–Beer–Law and by taking the attenuation lengths of the electrons of all involved peaks in all of the overlying layers into account [28]. As can be seen from the results of Fig. 9b, a layer thickness between 4.5 and 5 nm, averaged over the 400 μm spot size of the X-ray beam, could be determined. This layer thickness was finally confirmed on selected regions by comparative TEM measurements (not shown).

craters and positions 2 and 4 are on located on the plateaus. The topography in the valleys is much rougher than those of the plateaus

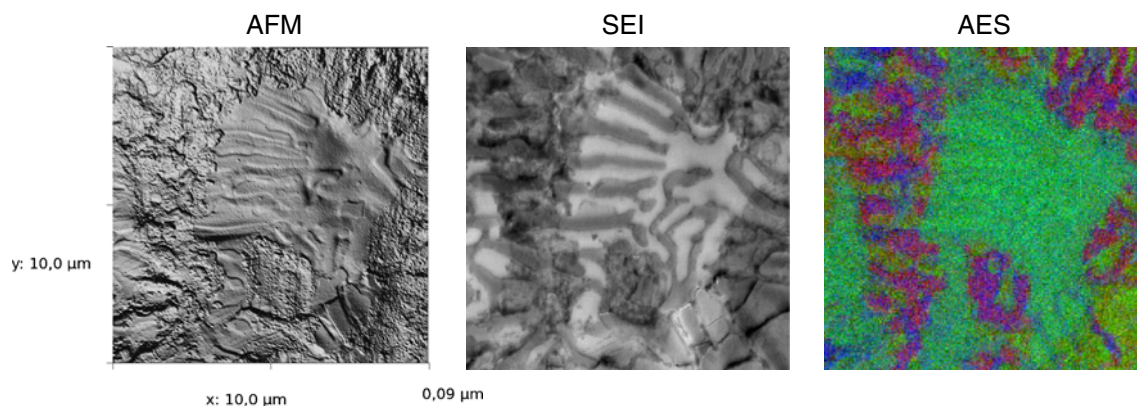


**Fig. 7** Position 1 from Fig. 6 is mapped again with AES. The topography of the AFM scan is matching perfectly with the elemental information from the AES mapping (Zn red, Mg green, Al blue)

## Discussion

The results shown above can be combined with already existing knowledge to build a model explaining the formation and structure of oxide layers on ZnMgAl coatings produced by hot dip galvanisation. In detail, the to-be-coated steel sheet passes through a bath of molten Zn–Mg–Al alloy with a composition of 96 wt.% Zn, 2 wt.% Mg and 2 wt.% Al. When the steel sheet is pulled out of the bath a ZnMgAl layer remains on the steel surface still in a molten, liquid state. Within this layer, the most oxygen affine elements immediately react with oxygen from the air of the surrounding environment and the reaction products precipitate and segregate on the surface to form the oxidic layer on the top. This process is already described for the formation of  $\text{Al}_2\text{O}_3$  oxide layers on the surface of standard hot dip galvanized zinc coatings emerging from coating baths containing only as few as 0.2 wt.% Al [23]. The

following basic chemical reactions can now potentially occur in the present material system:



From the Ellingham diagram, it can be found that Mg, as the most oxygen affine element in the ZnMgAl system, is followed directly by Al with the second highest affinity to oxygen [29]. In detail, the relative differences in the standard free energies of formation of oxides  $\Delta G^\circ$  between reactions 1, 2 and 3 are constant in the temperature window between 0 °C and 1,000 °C, thus including the temperature conditions under which the coatings were produced. However, the difference  $\Delta G^\circ$  between ZnO formation 1 and MgO formation 2 is approximately  $500 \text{ kJ mol}^{-1} \text{ O}_2$  as taken from the Ellingham diagram, much higher than the difference between MgO (Eq. 2) and  $\text{Al}_2\text{O}_3$  formation (Eq. 3) with only  $100 \text{ kJ mol}^{-1} \text{ O}_2$ . Hence, one could expect a formation of oxides on the surface with high magnesium and aluminium and low zinc content. This theoretical prediction is matching the experimental results, as the AES depth profiling results in Fig. 3 show Mg and Al oxides on the surface, but no Zn oxide. Moreover, the concentration of Mg oxide is significantly higher than the Al oxide concentration. In a similar way, the AR-XPS results of Fig. 9a show a higher Mg than Al concentration. However, this result has to be handled with care since the XPS peak intensities were not divided into oxidic and metallic contributions, and in the AES depth profile a higher Mg-to-Al metal ratio was found, an effect which could influence the AR-XPS result as well.

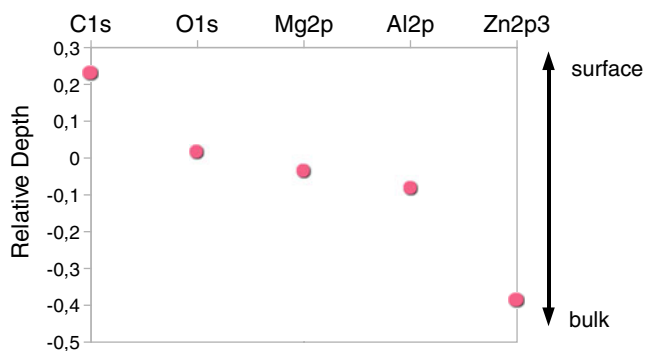


**Fig. 8** Relative depth plot of the measured elements by XPS on the surface of a non-skin passed ZnMgAl-coated steel. The  $y$ -axis corresponds to the average depth position where the respective element signal relatively to the other elements is found. The whole depth of information is limited by the inelastic mean free path of the involved electrons coming from a range of about 6 nm



Directly after its formation, the oxidic layer on the surface can be regarded as solid, because the considered Al and Mg compounds, namely MgO, Al<sub>2</sub>O<sub>3</sub>, have melting points above 2,000 °C. Furthermore, we have previously found indications—by analysing high energy resolution XPS spectra of Mg—for the formation of an alternative compound with high melting point, namely MgAl<sub>2</sub>O<sub>4</sub> spinel (Eq. 4) inside the MgAl oxidic layer [30].



The formed solid oxide layer can then prevent further oxidation of the zinc coating. This is in good agreement

with the AES depth profiling results shown in Fig. 3 where no ZnO was detected. The thickness of the oxide layer is uniform as shown in the Auger mappings of Fig. 4. The thickness was also measured via XPS as depicted in Fig. 9b and confirmed the findings of the Auger mapping. When the oxidic layer has built up, the underlying Zn metal layer is still liquid and solidifies later during cooling with typical Zn dendrite structures, Al dendrites and the binary and ternary eutectic, as shown in Fig. 1. A confirmation for this part of the model can be found in the fact that the surface oxides are not following the intermetallic structures underneath, as proven in Figs. 4 and 5. Also, the smoothness of the pristine surface, shown in the AFM scans of Fig. 6, is an indicator for the early oxide formation, otherwise the roughness of the surface would be higher if the dendrite structures are formed before.

The next step within the production process is the skin passing procedure. The ceramic MgAl oxidic layer is supposed to be harder and more brittle than the underlying metals and intermetallic alloys in the body of the coating. Therefore, it is assumed that the smooth oxide layer breaks into fragments which can partially be pressed into the metal on sites where the skin passing roll produces the imprints. In Fig. 7, such a small remaining fragment of the top oxidic layer, which is pressed into bulk material, is shown. The small brighter spots in the crater in the upper right picture of Fig. 5 directly show the distribution of these fragments. In addition, for the majority of the area in the imprinted craters, the metallic constituents appear on the surface, as proven in the AES mapping of Fig. 5. On the inhomogeneous metal surface, native oxide layers will be formed immediately (due to contact with air or rolling emulsion), but these passive layers are much thinner than the pristine MgAl oxide layer, resulting from a low, near-ambient temperature during the skin passing procedure. All these considerations are strictly only valid for equilibrium conditions and do not take kinetic effects or different reaction paths into account.

However, there are still open questions in the discussed model: By regarding the Ellingham diagram, one would expect gradients in the Mg and Al concentrations when going into the depth of the shallow surface layer, namely a higher Mg concentration on the surface of the MgAl oxide layer and a higher Al concentration towards the interface region between the surface oxide layer and bulk of the coating. Indeed, the relative depth plot of Fig. 8 from the ARXPS data indicates that the centre of the Al signal is situated in average below, but very close, to the centre of the Mg signal. This aspect has to be further clarified and is currently topic of our ongoing studies (Fig. 9).

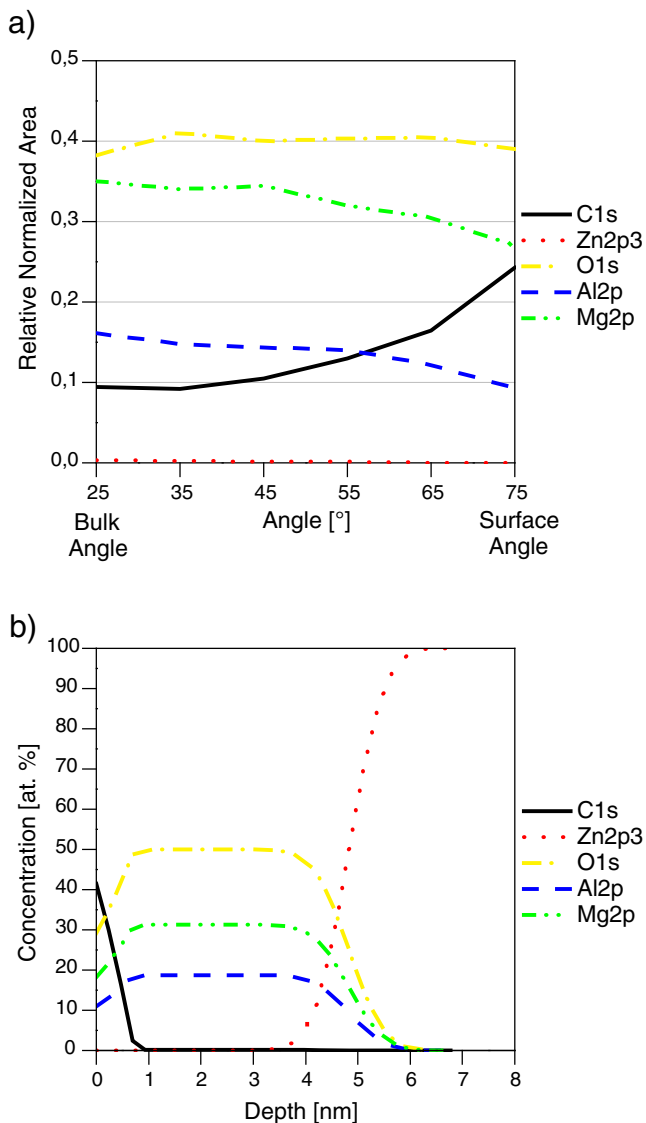


**Fig. 9** Graph a shows the measured relative intensities (normalized to 1) for six different angles. Graph b shows the result of a calculation on the basis of a three-layer model of Zn, MgAl oxide and C. The thickness of the MgAl oxide layer is determined to be between 4.5 and 5 nm

## Conclusions and outlook

In this work, the surface of ZnMgAl coatings produced by hot-dip galvanizing of steel sheets was analysed for the first time in depth by combining AES, ARXPS and AFM in order to shed light onto possible influences of the outermost oxide-layer in case of, e.g. initial corrosion attack, based on the special kind of surface structure, surface morphology or chemical composition. As a result, a thin, smooth Mg–Al-based oxide layer was found on the surface of the coating by AES depth profiling. The lateral distribution of this layer was proven by AES mapping to be homogeneous. The thickness of the layer lies between 4.5 and 5 nm, as measured by ARXPS. On skin passed samples, it could be confirmed via combined AFM measurements and AES element mappings that this layer is destroyed in the imprinted regions, whereas on the rest of the surface of the coating this layer is still present. Furthermore, the topography of the oxide layer was found to be significantly smoother than the surface inside the imprint regions, as determined by AFM. According to the results of the AES measurements, the surface oxide layer contains more Mg than Al oxidic compounds, being in good agreement with the complementary XPS results.

On the basis of the obtained results, a model of the forming mechanism of the coating was proposed to explain the observed chemical composition and the resulting topographic structure of the surface of the ZnMgAl coatings.

As an outlook, for the verification of included spinel structures in the MgAl oxide layer, TEM and selected area electron diffraction measurements are proposed and will follow in case that the layer is (partly) crystalline. In a similar way, secondary ion mass spectroscopy could be used to find indications for a spinel structure. For proving the proposed gradient of the Mg and Al concentrations, more surface-sensitive tools will be applied. This could be done by AES depth profiling and using the LVV or MVV Auger peaks of Zn, Mg and Al with energies below 100 eV. The inelastic mean free path of electrons in this energy range is far lower than of the KLL or LMM transitions being in the energy range between 1,000 and 1,400 eV, so the information depth becomes shallower. An alternative approach, as suggested by Tsutsumi et al. [31], is related to the application of a low-angle incident primary electron beam for Auger analysis in order to become more surface-sensitive.

**Acknowledgements** The financial support by the Federal Ministry of Economy, Family and Youth and the National Foundation for Research, Technology and Development is gratefully acknowledged (Christian Doppler Laboratory for Microscopic and Spectroscopic Material Characterisation, CDL-MS-MACH), as well as the financial support by the Austrian Research Promotion Agency (ZnMg hot-dip galvanized steel strip and processing and Bridge Project “Surface and interface analytics for steel composites”).

## References

1. Tano K, Higuchi S (1985) Development and properties of zinc–aluminum alloy coated steel sheet with high corrosion resistance (Super Zinc). Nippon Steel Technical Report 25:29–37
2. Tanaka S, Honda K, Takahashi A, Morimoto Y, Kurosaki M, Shindo H, Nishimura K, Sugiyama M (2001) The performance of Zn–Al–Mg–Si hot-dip galvanized steel sheet. Proc Galvatech 2001, Brussels, Belgium: 153–160
3. Nishimura K, Shindo H, Kato K, Morimoto Y (1998) Microstructure and corrosion behaviour of Zn–Mg–Al hot-dip galvanized steel sheet. Proc Galvatech 1998, Chiba, Japan: 437–442
4. Komatsu A, Tsujimura T, Watanabe K, Yamaki N, Andoh A, Kittaka T (1999) Hotdip Zn–Al–Mg coated steel sheet excellent in corrosion resistance and surface appearance and process for the production thereof, Nisshin Steel Corporation, Patent EP0905270
5. Hagler J, Angeli G, Ebner D, Luckeneder G, Fleischhanderl M, Schatzl M (2008) New zinc–magnesium–alloy coatings for building and construction industry. Proc Eurosteel 2008, Graz, Austria: 1–6
6. Faderl J, Angeli G, Luckeneder G, Tomandl A (2008) Thinner Zinc-based Coatings with improved corrosion protection – A contradiction? Proc SCT 2008, Wiesbaden, Germany: 1–8
7. Vlot M, Bleeker R, Maalman T, van Perlstein E (2006) MagiZinc™: a new generation of hot-dip galvanized products. Proc Galvanized Steel Sheet Forum, ILZRO and IZA, Duesseldorf, Germany
8. Bendick O, Keller M, Meurer M, Nabbefeld-Arnold E, Zeizinger S (2008) ZMg EcoProtect\_ – neue Beschichtung für einen hochwertigen Korrosionsschutz. TyssenKrupp techforum 1:16–21
9. Tsujimura T, Komatsu A, Andoh A (2001) Influence of Mg content in coating layer and coating structure on corrosion resistance of hot-dip Zn–Al–Mg alloy coated steel sheet. Proc Galvatech 2001, Brussels, Belgium: 145–152
10. Yamamoto S, Kumon F, Taomoto T, Entani H (2007) Corrosion Resistance of repainted Zn–6%Al–3%Mg alloy coated steel sheet. Proc Galvatech 2007, Osaka, Japan: 659–664
11. Ishikawa T, Ueda M, Kandori K, Nakayama T (2007) Air permeability of the artificially synthesized Zn–Al–Mg-alloy rusts. Corros Sci 49:2547–2556
12. Schuerz S, Luckeneder GH, Fleischhanderl M, Mack P, Gsaller H, Kneissel AC, Mori G (2010) Chemistry of corrosion products on Zn–Al–Mg alloy coated steel. Corros Sci 52:3271–3297
13. Schuerz S, Fleischhanderl M, Luckeneder GH, Preis K, Haunschmied T, Mori G, Kneissel AC (2009) Corrosion behaviour of Zn–Al–Mg coated steel sheet in sodium chloride-containing environment. Corros Sci 51:2355–2363
14. Hosking N, Ström M, Shipway P, Rudd C (2007) Corrosion resistance of zinc–magnesium coated steel. Corros Sci 49:3669–3695
15. Volovitch P, Allely C, Ogle K (2009) Understanding corrosion via product characterization: I. Case study of the role of Mg alloying in Zn–Mg coating on steel. Corros Sci 51:1251–1262
16. Chen S, Yan F, Xue F, Yang L, Liu J (2010) X-ray photoelectron spectroscopy investigations of zinc–magnesium alloy coated steel. Mat Chem and Phys 124:472–476
17. Kwak H, Chaudhuri S (2011) Cationic doping of MgO surfaces to build corrosion protection in Mg alloys. J Alloys Compd 509:8189–8198
18. Mohapatra D, Sarkar D (2007) Preparation of MgO–MgAl<sub>2</sub>O<sub>4</sub> composite for refractory application. J Mater Process Technol 189:279–283
19. Petot C, Ducos M, Petot-Ervas G (1995) Thermal spray spinel coatings on steel substrates: influence of the substrate composition and temperature. J Eur Ceram Soc 15:637–642
20. Shimizu T, Asada H, Morikawa S (2009) Proc Asia-Pacific Galv. Conf., Jeju, Korea

21. Warnecke W, Angeli G, Koll T, Nabbeled-Arnold E (2008) Entwicklungen in der Umformtechnik-Leistungsspektrum moderner Zink-Magnesium Schmelztauchüberzüge. *Stahl* 2008, Düsseldorf, Germany
22. Raab AE, Berger E, Freudenthaler J, Leomann F, Walch C (2011) ZnMgAl hot dip galvanised steel sheets—tribology and tool wear. *Proc Galvatech '11*, Genua, Italy
23. Faderl J, Strutzenberger J, Angeli J, Ritsche S, Szinyur J, Wolpers M (2002) Al-oxide layer on hot-dip galvanized steel sheet: Characterisation and influence on weldability. 44th MWSP Conference Proceedings, 6:845–852
24. Feliu S Jr, Barranco V (2003) XPS study of the surface chemistry of conventional hot-dip galvanised pure Zn, galvaneal and Zn–Al alloy coatings on steel. *Acta materialia* 51:5413–5424
25. De Bruycker E (2006) Zn-Al-Mg alloy coatings: thermodynamic analysis and microstructure related properties. PhD thesis, University of Ghent, Ghent, Belgium
26. Priewasser F (2008) Schicht- und Technologieentwicklung einer ZnAlMg Schmelztauchbeschichtung. PhD thesis, Vienna University of Technology, Vienna, Austria
27. Commenda C, Pühringer J (2010) Microstructural characterization and quantification of Zn–Al–Mg surface coatings. *Mat Char* 61:943–951
28. Watts J, Wolstenholme J (2003) An introduction to surface analysis by XPS and AES. Wiley, Chichester
29. Pawlek F (1983) *Metallhüttenkunde*, de Gruyter Verlag, Berlin-NewYork
30. Riener C, Preis K, Achammer E, Angeli G, Arndt M, Duchoslav J, Itani H, Stifter D, Hingerl K (2011) Nano-characterisation of the surface of HDG Zn–Al–Mg–coated steel sheets. *Proc Galvatech 2011*, Genua, Italy
31. Tsutsumi K, Nagasawa Y, Tazawa T (2007) Auger analysis using low angle incident electrons. *JEOL News* 42E No.1:40